Referenceless Reconstruction of Spatiotemporally Encoded Imaging Data: Principles and Applications to Real-Time MRI

Amir Seginer, Rita Schmidt, Avigdor Leftin, Eddy Solomon, and Lucio Frydman*

Purpose: Ultrafast sequences based on "Hybrid" spatiotemporal encoding (SPEN) replace echo-planar imaging's phase encoding "blips," while retaining a k-space readout acquisition. Hardware imperfections during acquisition may lead to ghosts and striped artifacts along the SPEN dimension; akin to echo-planar imaging's Nyquist ghosts, but weaker. A referenceless method to eliminate these artifacts in Hybrid SPEN is demonstrated.

Theory and Methods: Owing to its encoding in direct space, rather than reciprocal space, undersampling in SPEN does not generate an echo-planar-imaging-like aliasing, but instead lowers the spatial resolution. Hybrid SPEN data can be split into two undersampled signals: a reference one comprised of the odd-echos, and an even-echo set that has to be "corrected" for consistency with the former. A simple way of implementing such a correction that enables a joint high-resolution reconstruction is proposed.

Results: The referenceless algorithm is demonstrated with various examples, including oblique scans, large in vivo datasets from real-time dynamic contrast-enhanced perfusion experiments, and human brain imaging.

Conclusions: The referenceless correction enables robust single-scan imaging under changing conditions—such as patient motion and changes in shimming over time—without the need of ancillary navigators. This opens new options for real-time MRI and interactive scanning. **Magn Reson Med 72:1687–1695, 2014. © 2013 Wiley Periodicals, Inc.**

Key words: real-time magnetic resonance imaging; spatiotemporal encoding; referenceless reconstruction; dynamic contrast-enhanced magnetic resonance imaging

INTRODUCTION

Alternatives to echo-planar imaging (EPI) that use spatiotemporal encoding (SPEN) have recently been suggested (1,2). SPEN sequences maintain the single-excitation full two-dimensional (2D) acquisition nature of EPI, while overcoming inhomogeneity distortions and Nyquist ghosting along the low-bandwidth dimension. This robustness is achieved by replacing EPI's phase-encoding with a procedure that obviates the need for a Fourier transform (FT) along this dimension. A penalty associated with these sequences is the need for stronger gradients, and concomitantly higher specific absorption rates, than would be typically required by EPI for a similar scan. These demands can be eased by reducing the strength of the encoding gradient, G_e, but then image extraction with no accompanying resolution loss requires some form of super-resolved data processing along the SPEN dimension (3–5). This process requires a joint handling of data collected for all readout (RO) rows. As in the case of EPI, the joint processing of data collected under the oscillating gradient $\pm G_{ro}$ may introduce artifacts due to hardware imperfections. In EPI, these lead to Nyquist ghosts that are typically handled via calibration by an auxiliary reference (navigator) scan. Although usually smaller than their EPI counterparts, SPEN artifacts appear as "stripes" and "ghosts" after super-resolution (SR). As shown here, however, SPEN's nature as a direct-space imaging technique enables the elimination of these artifacts using the image data itself—without a navigator or reference scan. The present study introduces the principles that make such self-correction possible and gives examples of its use in a variety of instances including oblique scans, real-time in vivo perfusion imaging of mice kidneys, and brain imaging.

THEORY

Hybrid SPEN single-scan MRI relies on imparting the spins with a position-dependent quadratic phase $\varphi(y) = ay^2 + by + c$ along the low-bandwidth dimension. This is achieved by applying a frequency-swept pulse in the presence of a y-oriented encoding gradient G_e (1,2,6,7). In the one-dimensional (1D) case, assuming an acquisition gradient G_a along the same axis and discrete sampling time points t_m corresponding to k-space points $k_m = \gamma G_a t_m$, the signal due to spin density $\rho(y)$ is then

$$S(k_m) = \int \rho(y) e^{i(ay^2+by+k_m y)} dy, \qquad [1]$$

where constant phase terms are ignored for simplicity. One-dimensional SPEN can be extended into 2D in a number of different ways (1,2,8,9). Figure 1a depicts the "Hybrid SPEN" sequence assessed in this work, with the image k-

Chemical Physics Department, Weizmann Institute of Science, Rehovot, Israel, 76100

Grant sponsor: Kamin-Yeda Project 711237 (Israel Ministry of Trade and Industry); Grant sponsor: Helen and Martin Kimmel Award (Innovative Investigation); Grant sponsor: The generosity of the Perlman Family Foundation.

*Correspondence to: Lucio Frydman, Ph.D., Chemical Physics Department, Weizmann Institute, Rehovot, Israel 76100. E-mail: lucio.frydman@weizmann.ac.il

Additional Supporting Information may be found in the online version of this article.

Received 25 June 2013; revised 23 November 2013; accepted 25 November 2013

DOI 10.1002/mrm.25084

Published online 13 January 2014 in Wiley Online Library (wileyonlinelibrary.com).

encoded (Fourier) along the high-bandwidth RO direction and SPEN encoded along the low-bandwidth dimension.

The SPEN-encoded image can be extracted by the stationary phase approximation through $\rho(y) \propto S(k_m(y))$ with resolution limited to $\sqrt{\pi/|a|}$ (6,7). Several methods have been suggested to extract a higher resolution image from the integral Eq. 1. These include SR (3), localized FT (4,10), and deconvolution (5,11) algorithms. While the kind of analysis discussed here may apply to most of these reconstruction methods, we concentrate for conciseness on SR.

In SR, the integral in Eq. 1 is replaced by an expression that assumes a discretized object made of N elements

$$S(k_m) \approx \sum_{n=1}^{N} \hat{\rho}_n \overbrace{\int_{y_n-\delta}^{y_n+\delta} e^{i[ay^2+(b+k_m)y]}dy}^{A_{mn}}, \qquad [2]$$

where $\hat{\rho}_n$ is the approximate density in voxel n, y_n is the voxel's y-center, 2δ is the voxel's width, and A_{mn} is an element in the so-called "SR matrix" A. Eq. 2 can be rewritten in matrix form as $\boldsymbol{S} = A\hat{\boldsymbol{\rho}}$ (bold font denoting a vector). In principle, the imaged object can thus be determined by applying the pseudo-inverse $A^{+} = (A^{\dagger}A)^{-1}A^{\dagger}$ onto $\boldsymbol{S}$, where $A^{\dagger}$ is the complex transpose of A. In practice, however, the solution of $\boldsymbol{S} = A\hat{\boldsymbol{\rho}}$ is handicapped by A's typical ill-conditioning. For the final magnitude images presented in this work, the first iteration of the conjugate-gradients method suggested in (3) was used, which translates to applying $A^{\dagger}$ on $\boldsymbol{S}$ as an *approximate solution*. This use of $A^{\dagger}$ results in images with ghosts, typically of sample edges, but the ghosts were found to be reduced by applying Gaussian weighting to the rows of $A^{\dagger}$. (Ghosting of edges is an issue in other methods of solution as well). As the rows of $A^{\dagger}$ behave similarly to a sinc function (see Appendix, Eq. A2), the width 2σ of the Gaussian was chosen relative to the sinc's width

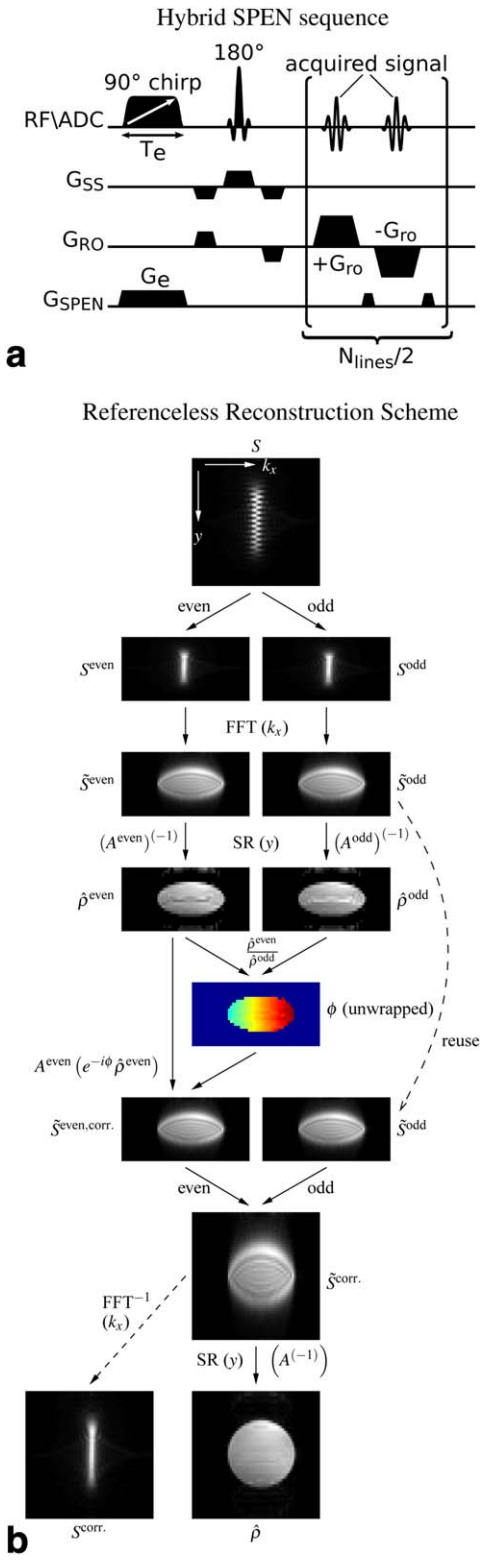

FIG. 1. a: 90°-chirp Hybrid SPEN sequence used in this study. b: Referenceless correction and reconstruction algorithm illustrated for a 114 mm diameter cylinder filled with doped H_2O. The referenceless algorithm is illustrated step-by-step from top to bottom. On top: the original data S collected as a function of (y, k_x) (columns and rows, respectively). The data are then split into even and odd rows, with each of the resulting sets S^{even} and S^{odd} being self-consistent. FT performed along the horizontal RO direction gives $\tilde{S}^{even}$ and $\tilde{S}^{odd}$ and is followed by SR reconstruction along the vertical SPEN direction resulting in two correct, but low-resolution, even/odd images of the same object: $\hat{\rho}^{even}$ and $\hat{\rho}^{odd}$. The phase difference ϕ between the two images ($e^{i\phi} = \hat{\rho}^{even}/\hat{\rho}^{odd}$) is then derived, and its (x, y) spatial dependence fit with a second degree polynomial. Using this fit, a corrected even image $\hat{\rho}^{even,corr.} = e^{-i\phi}\hat{\rho}^{even}$ (not shown) is found, and a corrected "signal" $\tilde{S}^{even,corr.}$ is derived through: $\tilde{S}^{even,corr.} = A^{even}(e^{-i\phi}\hat{\rho}^{even})$ (where the product $e^{-i\phi}\hat{\rho}^{even}$ is an entry by entry product such as .* in Matlab). Next, $\tilde{S}^{even,corr.}$ is rejoined with $\tilde{S}^{odd}$ to create a full corrected "signal" $\tilde{S}^{corr.}$. Applying SR (denoted $A^{(-1)}$) on this full and corrected "signal" produces the final reconstructed image $\hat{\rho}$. An inverse FT along the RO direction shows (bottom left) that the corrected signal $S^{corr.}$ no longer has echo time shifts (compare to S at top). Note, that although a 1D phase fit may suffice in this example, the algorithm described is general (see main text). [Color figure can be viewed in the online issue, which is available at wileyonlinelibrary.com.]

$2\pi/(2a\delta)$—the distance between the two central zeros. A factor of 0.8 was chosen, which from our experience lead to a good compromise between reducing ghosts and high final image resolution. (The factor of 0.8 translated to σ ranging from 13 to 20 pixels for the final images shown here.)

The use of RO gradients with alternating polarities is common to both 2D EPI and Hybrid SPEN, therefore, the same imperfections which lead to Nyquist ghost in EPI (12–14) also lead to artifacts (ghosts and stripes) in Hybrid SPEN (e.g., Fig. 2c). These imperfections are typically modeled as an extra shift in k-space between lines acquired during the opposite gradient polarities (13). In principle, EPI images generated from points sampled under each of the gradient polarities can be compared, their k-space shift corrected, and a final combined image generated. However, by using only same-polarity RO rows, the k-space interval along the phase-encoding is doubled. In EPI, this strategy would cause aliasing that would interfere with the analysis for objects larger than half the phase-encoding field-of-view (FOV). To resolve this issue, both reference-based techniques (12,15–17) and image-processing methods (12,18–20) have been proposed. This problem of aliasing, however, does not arise in SPEN MRI. Instead, separating the rows of opposite gradient polarities in Hybrid SPEN will still lead to two full-FOV images, albeit of lower resolution; this can be exploited as a basis for a referenceless (or self-referencing) corrective method. To better appreciate this option, assume a Hybrid SPEN MRI signal S_{mq} and final image $\hat{\rho}_{nq}$ with, respectively, $m = 1,\ldots,M$ points and $n = 1,\ldots,N$ pixels along the column/SPEN dimension—typically $M=N$, but not necessarily—and with $q = 1,\ldots,Q$ samples/pixels along the row/RO dimension. The resulting signal after FT along the RO direction shall be denoted as $\tilde{S}_{mq}$, which after SR applied to each column results in the final image $\hat{\rho}_{nq}$. To generate low-resolution images arising separately from the even or the odd signal rows (matching either of the gradient polarities), two new SR matrices A^{even} and A^{odd} are defined by replacing k_m in Eq. [2] with its even and odd subsets k_m^{even} and k_m^{odd}, respectively. To compare only the effects of the k_m^{even} vs. k_m^{odd} sampling, the same pixel positions y_n are used for both matrices, still covering the original full FOV, but with half (or lower) resolution, because each set has only half the sample points. Assuming a deviation k_Δ^{SPEN} of the even rows (along SPEN) small enough to fulfill $|k_\Delta^{\text{SPEN}}|\delta \ll 1$ (typically a reasonable assumption) it can be shown (see Appendix) that for $a\delta^2 \ll 1$ the two images $\hat{\rho}^{\text{even}}$ and $\hat{\rho}^{\text{odd}}$, from $\tilde{S}^{\text{even}}$ and $\tilde{S}^{\text{odd}}$, respectively, will differ in phase with negligible differences in their magnitude; i.e.

$$\frac{\hat{\rho}_{nq}^{\text{even}}}{\hat{\rho}_{nq}^{\text{odd}}} = e^{i\phi_{nq}}, \qquad [3]$$

where $e^{i\phi_{nq}}$ expresses the inconsistencies between the even and odd rows, and ϕ_{nq} should be linear in n and q. It is worth remarking, however, that the method described above for the final calculation of super-resolved (magnitude) images will not perform sufficiently well when dealing with this kind of cases, where preserving the fidelity of the phases is important. Still, it was found that a reliable phased SR reconstruction could be reached if the resolution of these even/odd reconstructed images was reduced below its maximum signal points. A factor of 0.9 was suitable for this reduction; for instance, if the original SPEN signal had $M=70$ rows, we would set the SR reconstruction for the even/odd images in Eq. 3 to have $N=32$ rows ($0.9\times 70/2$). As a consequence of this, the even/odd SR matrices are rectangular (35×32 in our example); the problem is thus overdetermined, and its stability is improved.

Based on all these considerations, the relation in Eq. [3] above can be used to achieve a consistent set of data by defining a corrected even image

$$\hat{\rho}_{nq}^{\text{even,corr.}} \equiv e^{-i\phi_{nq}}\hat{\rho}_{nq}^{\text{even}}, \qquad [4]$$

to which corresponds a corrected even signal

$$\begin{aligned}\tilde{S}^{\text{even,corr.}} &= A^{\text{even}}\hat{\rho}^{\text{even,corr.}} \\ &= A^{\text{even}}\left[\begin{pmatrix}\hat{\rho}_{1,1}^{\text{even,corr.}}\\ \hat{\rho}_{2,1}^{\text{even,corr.}}\\ \vdots \\ \hat{\rho}_{N/2,1}^{\text{even,corr.}}\end{pmatrix}\begin{pmatrix}\hat{\rho}_{1,2}^{\text{even,corr.}}\\ \hat{\rho}_{2,2}^{\text{even,corr.}}\\ \vdots \\ \hat{\rho}_{N/2,2}^{\text{even,corr.}}\end{pmatrix}\cdots\begin{pmatrix}\hat{\rho}_{1,Q}^{\text{even,corr.}}\\ \hat{\rho}_{2,Q}^{\text{even,corr.}}\\ \vdots \\ \hat{\rho}_{N/2,Q}^{\text{even,corr.}}\end{pmatrix}\right].\end{aligned} \qquad [5]$$

Combining this corrected even signal with the original odd signal, creates a full self-consistent set

$$\tilde{S}^{\text{corr.}} = \left[\begin{pmatrix}\tilde{S}_{1,1}^{\text{odd}}\\ \tilde{S}_{1,1}^{\text{even,corr.}}\\ \tilde{S}_{2,1}^{\text{odd}}\\ \tilde{S}_{2,1}^{\text{even,corr.}}\\ \vdots\end{pmatrix}\cdots\begin{pmatrix}\tilde{S}_{1,Q}^{\text{odd}}\\ \tilde{S}_{1,Q}^{\text{even,corr.}}\\ \tilde{S}_{2,Q}^{\text{odd}}\\ \tilde{S}_{2,Q}^{\text{even,corr.}}\\ \vdots\end{pmatrix}\right], \qquad [6]$$

from which one can get a full $N\times Q$, artifact-free, corrected image

$$\hat{\rho}^{\text{corr.}} = A^{(-1)}\tilde{S}^{\text{corr.}}, \qquad [7]$$

where $A^{(-1)}$ denotes the operation used for SR (in our case, as described above, the first iteration of the conjugate-gradients method, including Gaussian weighting of the columns of A).

The general process described above can be refined when a purely 1D RO phase correction is expected; typically in nonoblique scans. In such a case, a 1D phase ϕ_q can be determined from Eq. 3, and the phase correction can be applied directly to $\tilde{S}^{\text{even}}$, bypassing the SR imperfections of transforming $\tilde{S}^{\text{even}}$ to $\hat{\rho}^{\text{even}}$ and then $\hat{\rho}^{\text{even,corr.}}$ to $\tilde{S}^{\text{even,corr.}}$. Despite the 1D phase fit, the ratio $\tilde{S}_{nq}^{\text{even}}/\tilde{S}_{nq}^{\text{odd}}$ cannot replace $\hat{\rho}_{nq}^{\text{even}}/\hat{\rho}_{nq}^{\text{odd}}$ in Eq. 3. This is because the 1D

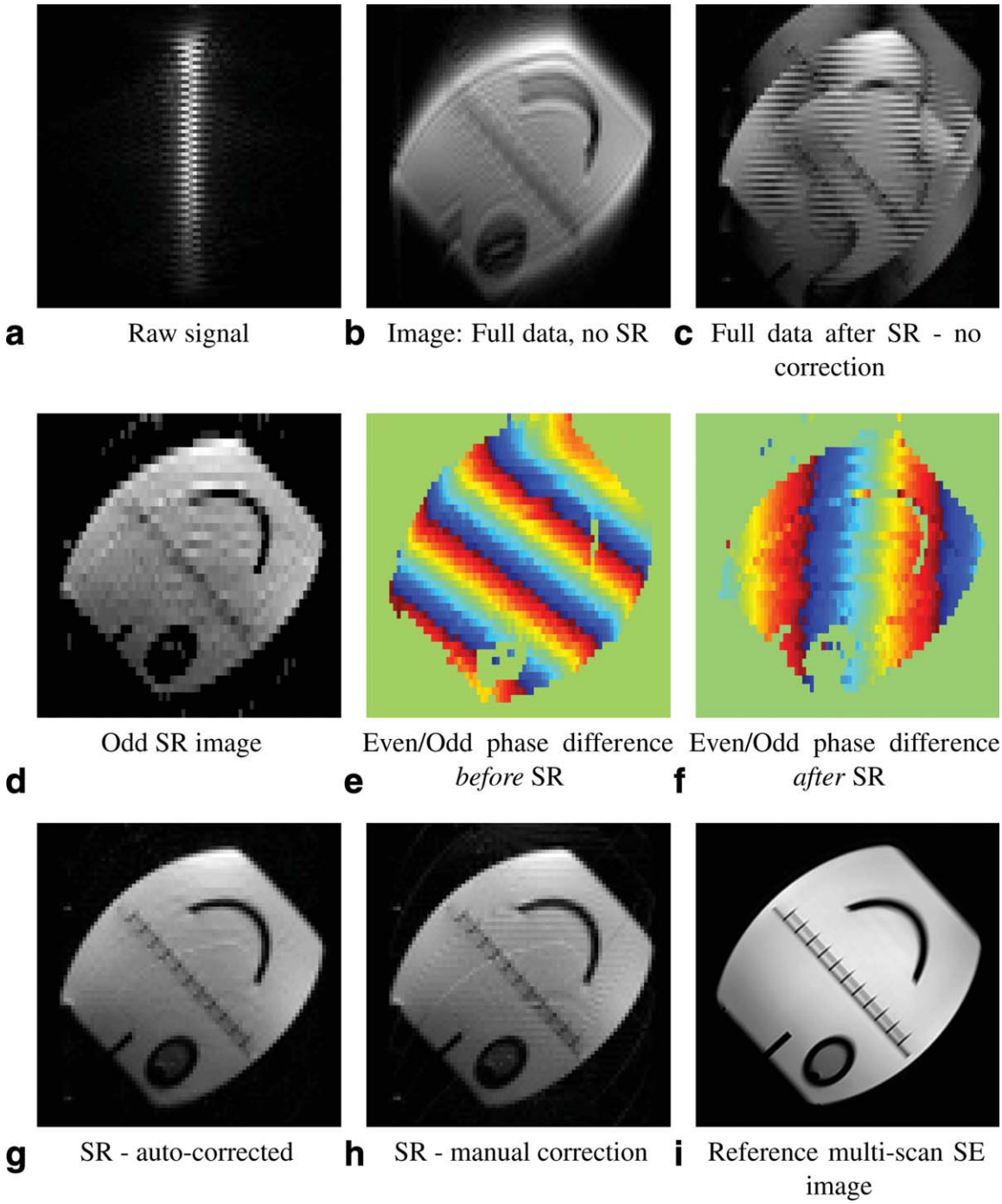

FIG. 2. Demonstrating the process of referenceless Hybrid SPEN auto-correction on an ACR phantom. a: Acquired signal showing a clear even/odd echo shift. b: Resulting image after FT along the horizontal RO direction (before SR). c: Image arising when SR follows the FT with no further corrections. d: SR image generated from the odd rows only, with regions of low-trust masked. e: Relative phase map of even/odd images *before* SR ($-\pi$ to $+\pi$ scale), with regions of low-trust masked. f: Relative phase map of even/odd images after SR, once more with $-\pi$ to $+\pi$ scale and regions of low-trust masked. g: Final autocorrected SR image. h: The result of a manual correction of the same data. i: High-resolution SE image. The Hybrid SPEN sequence used the following scan parameters: FOV = 27 × 27 cm^2 (double-oblique plane: 45° between axial and sagittal, and a 45° in plane rotation), slice thickness = 5 mm, acquisition matrix = 80 × 80, BW per pixel (RO) = 3.9 kHz, TE = 9–121 ms, and chirp duration = 56 ms using a 0.04 G/cm gradient. Total scan duration was 121 ms. The reference SE scan used the same FOV and scan plane as the Hybrid SPEN. Its scan parameters were: acquisition matrix = 384 × 384, BW per pixel (RO) = 219 Hz, TE = 71 ms, TR = 1.5 s, echo train length = 18, and averages = 2.

fit must also determine the constant even/odd phase difference (14), but $\tilde{S}^{\text{even}}$ and $\tilde{S}^{\text{odd}}$ (and, therefore, $\tilde{S}^{\text{even}}_{nq}/\tilde{S}^{\text{odd}}_{nq}$) include additional object dependent phases along the SPEN dimension. After SR these object dependent phases are absent in $\hat{\rho}^{\text{even}}$ and $\hat{\rho}^{\text{odd}}$. (Although not a truely 1D phase dependent case, the pronounced

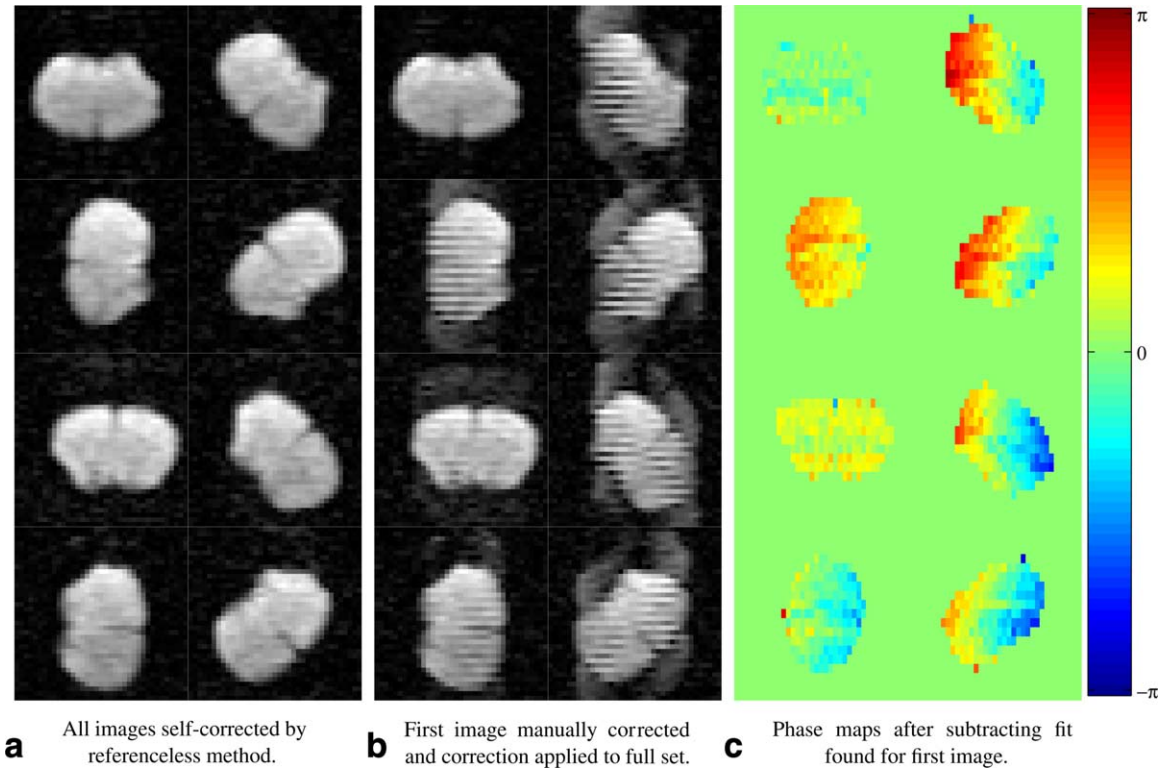

FIG. 3. Referenceless correction for inplane rotation of the RO and SPEN axes. A fixed mouse brain was repeatedly scanned, but with the RO and SPEN axes rotated inplane in 4° increments (eight of 89 orientations shown). a: Resulting images when the referenceless correction is performed per image. b: Resulting images when applying the manual correction of the first image (top left) to all images. c: Phase maps of ρ^{even}/ρ^{odd}, after removing first-order fit for first image (with strong linear phase along RO) and after masking of noisy regions; the 2D phase dependence is clear. Images shown are a zoom-in — 37 × 37 pixels out of 70 × 70 (37 × 19 out of 70 × 35 for phase maps). For the magnitude images, windowing was applied along the RO direction to improve signal to noise ratio. Scan parameters were: FOV = 25 × 25 mm^2, slice thickness = 2 mm, acquisition matrix = 70 × 70, BW per pixel (RO) = 3.57 kHz, flip angle = 90°, TE = 5–64 ms, TR = 1.1 s, chirp duration = 27.7 ms using a 0.9 G/cm gradient. (Full movies of all images can be found in the Supporting Information SI1a, SI1b, and SI1c.) [Color figure can be viewed in the online issue, which is available at wileyonlinelibrary.com.]

effect of SR on the phase behavior can be seen in comparing the phase difference in Fig. 2e before SR to the phase difference in Fig. 2f after SR.)

The referenceless SPEN-correcting algorithm just described is depicted schematically in Figure 1b.

METHODS

The referenceless algorithm was tested using the Hybrid SPEN sequence in Figure 1a. Scans were performed on different machines and different objects/subjects. In all cases, $a\delta^2$ was calculated and found to be smaller than 0.05, obeying the condition $a\delta^2 \ll 1$. In all cases, the general 2D phase fit of ϕ_{nq} from Eq. 3 was performed in steps: first removing the dominant linear phase along the RO direction, and only then determining the remaining 2D dependence.

Phantom tests were performed using an American College of Radiology (ACR) MRI Accreditation Program phantom scanned on a 3T Siemens (Siemens Healthcare, Germany) TIM TRIO scanner with a four-channel head coil. Both Hybrid SPEN and standard high-resolution SE images were collected. A double-oblique scan plane was chosen (45° between axial and sagittal, with a 45° inplane rotation) to emphasize the even/odd inconsistency along the SPEN direction (13). The performance of the referenceless algorithm was compared to that of the "manual" method previously used by our group (3,9,21); a method involving interactive visual alignment of the even/odd datasets in the raw signal *S*.

The effect of changing the scan plane on the quality of the reconstruction was tested using a fixed mouse brain in a 7T 300/89 Varian VNMRS vertical system (Agilent), scanned with a 30 mm Millipede probe. A Hybrid SPEN scan (nonoblique slice) was performed repeatedly while the RO and SPEN directions were successively rotated inplane by 4° increments per image. These tests then compared applying the referenceless reconstruction to each image, against results arising upon applying to all images the same "manual" correction found for the first image.

The referenceless algorithm was also tested on real-time in vivo animal perfusion experiments; these were performed in accordance with protocols approved by the Weizmann Institute's Animal Care and Use Committee. These experiments were chosen to showcase Hybrid SPEN's single-scan imaging capabilities in a challenging region—mice kidneys at 9.4 T—as well as to demonstrate the algorithm's automatic capability for large datasets. Experiments were conducted on a 9.4T Biospec scanner (Bruker, Germany) using a linear volume transmitter

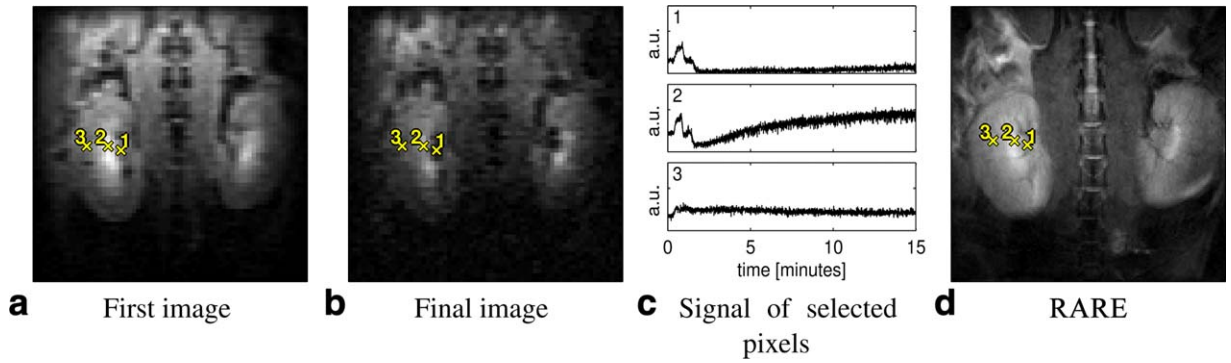

FIG. 4. DCE MRI of mouse kidneys using Hybrid SPEN. a: First image of the complete DCE dataset, recorded prior to reaching steady-state magnetization conditions and prior to contrast agent injection. b: Final image of the DCE (image 3000 after 15 mins). c: DCE time courses of the pixels marked on panels a and b. d: Reference image acquired using RARE, showing the approximate positions of the selected pixels. Time courses show the regional variation of the Gd-DTPA effect on the signal: 1–renal artery (upper); 2–medulla (center); and 3–cortex (bottom). Noise in the time courses, due to pixel displacement, was reduced by discarding 800 images with large kidney motion. The first image a is also not included, due to much higher signal (3.5–10 times higher than the peak signal at around 40 s). Each group of 1000 images took approximately 16 s to analyze and reconstruct once data was loaded into memory (Matlab 7.12, 32 bit, on an Intel Core i5 laptop with 8 GB of memory). All scans used a FOV of 30 × 30 mm^2, slice thickness of 2 mm, as well as fat suppression. The Hybrid SPEN parameters were: acquisition matrix = 36 × 100 (36 along RO), BW per sample (RO) = 2.78 kHz, flip angle = 90°, TE = 2–52 ms, TR = 300 ms, and chirp duration = 25 ms using a 0.78 G/cm gradient. A final image resolution of 64 × 64 was set to increase RO resolution, while also increasing SNR at the expense of SPEN resolution. The RARE scan parameters were: acquisition matrix = 128 × 128, BW per pixel (RO) = 391 Hz, TE = 42.7 ms, TR = 1.5 s, RARE factor = 8, and averages = 2. (A movie from all 3000 images can be found in the Supporting Information SI2.) [Color figure can be viewed in the online issue, which is available at wileyonlinelibrary.com.]

with a 2 cm surface coil receiver. Female Institute of Cancer Research (ICR) mice were anesthetized, and after the imaging experiment began, they were injected over 1–2 s with gadolinium-diethylene-triamine-pentaacetic-acid (Gd-DTPA) contrast agent Magnetol in phosphate buffered saline (PBS). A total of 3000 Hybrid SPEN images were acquired over 15 mins. Reconstruction was implemented using the referenceless method, and time traces were extracted from the resulting images for selected pixels. A single RARE scan with higher resolution was also performed for reference.

Finally, the reconstruction algorithm was also applied to volunteer brain images, scanned on the same 3T Siemens setup as the ACR phantom above. Experiments were performed after obtaining suitable written informed consents and following procedures approved by the Internal Review Board of the Wolfson Medical Center (Holon, Israel). Two scans were performed: a Hybrid SPEN sequence and a standard high-resolution spin-echo scan. Unlike all previous examples, the Hybrid SPEN in this case used ramp sampling, thus allowing to shorten the scan. Regridding was applied prior to the even/odd correction.

RESULTS

Figure 2 shows various aspects associated with the referenceless reconstruction for a single-scan oblique image of the ACR phantom. Figure 2a shows the raw acquired signal (magnitude) evidencing the even/odd echo shift. Figure 2b shows the low-resolution (magnitude) image obtained by FT along the RO (horizontal) direction. As no SR is applied at this stage, the even/odd inconsistency is not a serious source of artifacts. This is unlike the result in Figure 2c, which was obtained by applying SR directly to the data without any even/odd corrections. The artifact-free low resolution image obtained upon applying SR onto the odd rows can be seen in Figure 2d. The phase difference between the even/odd images is shown in Figure 2e before SR is applied, and in Figure 2f after SR is applied. The latter exhibits a slight but noticeable 2D phase dependence. The final result of the automatic referenceless method is shown in Figure 2g. A correction using only a linear 1D phase along the RO direction was also performed (not shown), but resulted in the emergence of stripe artifacts. For comparison, Figure 2h shows the image arising from the same raw data after applying our previous "manual" correction method (3), that includes a visual alignment of the even/odd echos. A high-resolution multiscan SE image is also shown in panel 2i.

A further comparison of the manual vs. the new "referenceless" method is shown in Figure 3, for a fixed mouse brain subject to in-plane rotations (in 4° increments) of the imaging RO and SPEN gradients. Figure 3a shows the result of applying the referenceless correction to a representative number of sample images/rotations; each image self-corrected according to its own phase map. Figure 3b shows the same set of images when the manual corrections found for the first set is applied to all other images in a "blind" mode (of the kind that would be used when dealing with a large data set). The change in the phase maps from an initial first-order fit is given in Figure 3c demonstrating the necessity of a 2D phase fit. The figure clearly shows the benefits of implementing per-image corrections under changing geometries and orientations. Full movies of the ensuing "rotations" can be found in the Supporting Information SI1a, SI1b, and SI1c.

Figure 4 shows "real-time" results for the mapping of the dynamic contrast-enhanced (DCE) perfusion of Gd-

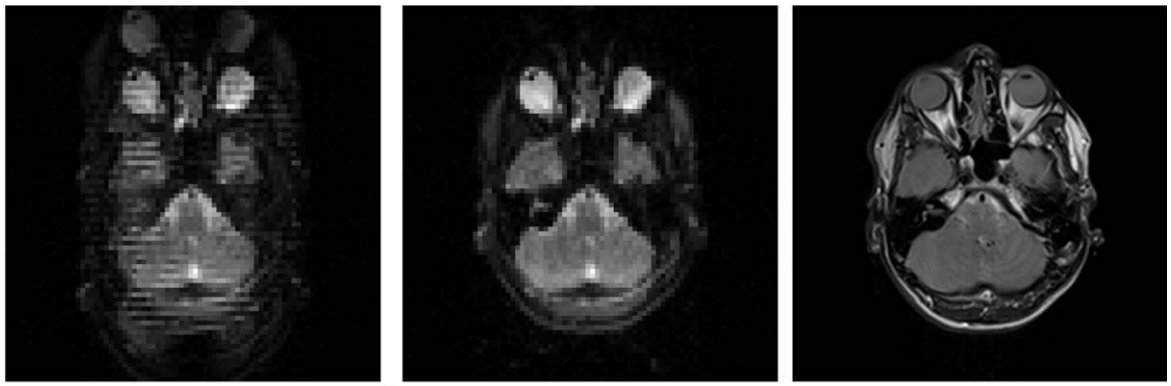

FIG. 5. a: Hybrid SPEN volunteer brain image reconstructed by SR, but without corrections, b: Hybrid SPEN SR image with a referenceless correction applied. c: High-resolution multiscan SE image, for reference. Scans were performed at the same position with FOV = 24 × 24 cm^2, and slice thickness of 3 mm. The Hybrid SPEN used ramp sampling for a final acquisition matrix of 80 × 80, BW per pixel (RO) = 2.5 kHz, and a 90° flip angle. Regridding was performed prior to referenceless corrections. The Hybrid SPEN had a TE of 9–89 ms, with chirp duration 40 ms using a 0.063 G/cm gradient. Total scan duration was 91 ms. The SE acquisition matrix was 384 × 198, BW per pixel (RO) = 219 Hz, TE = 71 ms, TR = 1.5 s, echo train length = 18, and averages = 2.

DTPA in mouse kidneys. The first Hybrid SPEN image of the DCE dataset is given in Figure 4a while the final image, after 15 mins of data acquisition, is shown in Figure 4b. Time courses of three representative pixels chosen to coincide with the renal artery, the renal medulla, and the renal cortex, are shown in Figure 4c. The results show the expected behavior: the arterial perfusion (time course 1) is characteristic of a rapid bolus passage; the deep medulla region (time course 2) displays the largest contrast, with contributions from both the first pass arterial perfusion as well as a slow increase in T_1 weighting owing to Gd-DTPA accumulation in the nephrons; finally, in the outer cortex region (time course 3), the contrast level rises rapidly due to first pass kinetics, but then remains at a near-constant plateau as the acquisition duration is too short for the contrast agent to clear.

Finally, Figure 5 presents Hybrid SPEN reconstruction results of a volunteer brain scan. As in the case of the phantom, a multiscan SE image was also scanned for reference. The benefits of the referenceless method are evident once again, even in this highly optimized setting oriented for functional-MRI.

DISCUSSION

The results hereby presented show the suitability of the referenceless algorithm introduced in this article for correcting Hybrid SPEN signals in an automated fashion, without demanding the collection of ancillary data. The benefits of the referenceless method are clearly seen in Figure 3, where the scan conditions change with changing scan orientation: the referenceless method compensates for these changes on a per image basis. The convenience of the referenceless method is also illustrated by the perfusion experiments shown in Figure 4, where the acquisition of thousands of images taxes both the stability of the spectrometer system, and any kind of data processing that requires an interactive input. The referenceless processing algorithm provides an ideal tool for this, and could process all data in a real-time fashion without aid from navigators.

Over the course of this study, we tried several other SR corrective methods, including reference-based multiscan approaches of the kind normally used in EPI. These methods, however, performed worse than the referenceless variant described here—particularly for oblique scans. We suspect that this reflects slight differences between the base and the reference scans, making the referenceless approach a method of choice for processing Hybrid SPEN data.

Despite its proven performance, the referenceless method has potential limitations. As mentioned, its correction supports only k_Δ^{SPEN} errors fulfilling the condition $k_\Delta^{\mathrm{SPEN}}\delta \ll 1$. Although this demand was met in all the instances explored in this study, it might break down for ill-behaved systems or very poor hardware. The referenceless algorithm also depends on the quality of the polynomial fit that is achieved for the even/odd phase differences. This in turn will depend on a proper phase unwrapping, and on a suitable masking/weighting of low-trust regions. Furthermore, as the referenceless method uses SR internally to generate $\hat{\rho}^{\mathrm{even,corr.}}$ and from it $S^{\mathrm{even,corr.}}$ (while leaving S^{odd} untouched), using unstable or nonideal SR operations may have undesired effects (a recently published SR method (22) using compressed sensing may alleviate this, although such method is computationally much more intensive than the one here discussed).

CONCLUSIONS

A new referenceless algorithm was demonstrated for the automated correction of Hybrid SPEN sequences. This algorithm allows one to retrieve quality images from consecutive single scans under changing conditions without a need for collecting ancillary reference scans. Although the algorithm was exemplified for SPEN experiments relying on a 90° chirped excitation, the same considerations apply in the SR processing of data collected with other versions in this family of 2D MRI single-shot sequences (1,21,23). The addition of referenceless reconstruction to the rapid scan times of these methods may

assist in making Hybrid SPEN, a method-of-choice for real-time imaging in challenging regions. The referenceless reconstruction could also prove useful when using Hybrid SPEN sequences for other real-time application like diffusion studies or functional MRI. Similar concepts are being pursued in the realm of single-scan 2D MR spectroscopic data acquisitions.

APPENDIX—JUSTIFYING THE REFERENCELESS CORRECTION

To justify the referenceless algorithm, and especially Eq. 3, we assume that just as in EPI (13,24) imperfections during the acquisition will lead to constant but unknown k-space shifts k_Δ^{RO} and k_Δ^{SPEN}. Consequently, odd rows are still sampled at $k_y = k_m^{\mathrm{odd}}$ and $k_x = k_q$ along the SPEN and RO dimensions, respectively, but even rows are sampled at $k_y = k_m^{\mathrm{even}} + k_\Delta^{\mathrm{SPEN}}$ and $k_x = k_q + k_\Delta^{\mathrm{RO}}$. The k_Δ^{RO} shift leads, following a FT along the rows, to a linear phase $k_\Delta^{\mathrm{RO}} x_q$ along the RO direction. To handle the k_Δ^{SPEN}shift, a further expansion of the SR matrix A is needed. To derive this effect we make a variable change $y = y_n + s$, and the integral in Eq. 2 becomes

$$A_{mn} = e^{i[ay_n^2 + (b+k_m)y_n]} \int_{-\delta}^{\delta} e^{ia[s^2 + 2\left(y_n + \frac{b+k_m}{2a}\right)s]} ds. \qquad [A1]$$

Assuming that as^2 is always small enough, i.e., $|a\delta^2| \ll 1$, Eq. A1 can be approximated to zero order in $a\delta^2$ as

$$A_{mn} \approx 2\delta e^{i[ay_n^2 + (b+k_m)y_n]} \mathrm{sinc}\left[2a\delta\left(y_n + \frac{b+k_m}{2a}\right)\right] \begin{pmatrix} \text{zero} \\ \text{order} \end{pmatrix}. \qquad [A2]$$

From Eq. A2, the constant shift k_Δ^{SPEN} along the SPEN direction gives

$$\begin{aligned} \tilde{S}_{(m+\Delta^{\mathrm{SPEN}}),q} &\approx \sum_n \rho_{n,q} 2\delta e^{i[ay_n^2 + (b+k_m+k_\Delta^{\mathrm{SPEN}})y_n]} \\ &\qquad \mathrm{sinc}\left[2a\delta\left(y_n + \frac{b+k_m+k_\Delta^{\mathrm{SPEN}}}{2a}\right)\right] \\ &\approx \sum_n \rho_{n,q} e^{ik_\Delta^{\mathrm{SPEN}} y_n} 2\delta e^{i[ay_n^2 + (b+k_m)y_n]} \\ &\qquad \mathrm{sinc}\left[2a\delta\left(y_n + \frac{b+k_m}{2a}\right)\right] \\ &= \sum_n A_{m,n}\left(\rho_{n,q} e^{ik_\Delta^{\mathrm{SPEN}} y_n}\right), \end{aligned} \qquad [A3]$$

where we have dropped k_Δ^{SPEN} in the sinc argument of the second line because under all reasonable experimental conditions k_Δ^{SPEN} obeys $k_\Delta^{\mathrm{SPEN}}\delta \ll 1$, and we have already neglected a similarly small quantity $a\delta^2$ in establishing Eq. A2. Recalling the linear phase difference $k_\Delta^{\mathrm{RO}} x_q$ between odd and even rows, and allowing for a constant phase difference ϕ_0, we get

$$\tilde{S}_{m,q}^{\mathrm{odd.}} = \sum_n A_{m,n}^{\mathrm{odd}} \rho_{n,q} \qquad [A4a]$$

$$\begin{aligned} \tilde{S}_{m,q}^{\mathrm{even.}} &= \sum_n A_{m,n}^{\mathrm{even}}\left(\rho_{n,q} e^{i\phi_0} e^{ik_\Delta^{\mathrm{SPEN}} y_n} e^{ik_\Delta^{\mathrm{RO}} x_q}\right) \\ &\equiv \sum_n A_{m,n}^{\mathrm{even}}\left(\rho_{n,q} e^{i\phi_{n,q}}\right). \end{aligned} \qquad [A4b]$$

In other words, given the assumptions made, the difference between the low-resolution image retrieved from $\tilde{S}_{mq}^{\mathrm{odd}}$ and the one retrieved from $\tilde{S}_{mq}^{\mathrm{even}}$ is a linear 2D phase $e^{i\phi_{nq}} = e^{i(\phi_0 + k_\Delta^{\mathrm{SPEN}} y_n + k_\Delta^{\mathrm{RO}} x_q)}$. In practice, and to allow for minor deviations from the model just presented, a general 2D fit of the phase difference based on a second-order polynomial was used.

ACKNOWLEDGMENTS

The authors are grateful to Yuval Zur for helpful discussions on EPI reconstruction, to Dr. Sagit Shushan (Wolfson Medical Center), and to Dr. Edna Haran and the Weizmann MRI technician team, for assistance in the human imaging scans.

REFERENCES

1. Ben-Eliezer N, Shrot Y, Frydman L. High-definition, single-scan 2D MRI in inhomogeneous fields using spatial encoding methods. Magn Reson Imaging 2010;28:77–86.
2. Chamberlain R, Park JY, Corum C, Yacoub E, Ugurbil K, Jack CR Jr, Garwood M. Raser: a new ultrafast magnetic resonance imaging method. Magn Reson Med 2007;58:794–799.
3. Ben-Eliezer N, Irani M, Frydman L. Super-resolved spatially encoded single-scan 2D MRI. Magn Reson Med 2010;63:1594–1600.
4. Chen Y, Li J, Qu X, Chen L, Cai C, Cai S, Zhong J, Chen Z. Partial Fourier transform reconstruction for single-shot MRI with linear frequency-swept excitation. Magn Reson Med 2013;69:1326–1336.
5. Cai C, Dong J, Cai S, Li J, Chen Y, Bao L, Chen Z. An efficient deconvolution reconstruction method for spatiotemporal-encoding single-scan 2d MRI. J Magn Reson 2013;228:136–147.
6. Shrot Y, Frydman L. Spatially encoded NMR and the acquisition of 2D magnetic resonance images within a single scan. J Magn Reson 2005;172:179–190.
7. Tal A, Frydman L. Single-scan multidimensional magnetic resonance. Prog Nucl Magn Reson Spectrosc 2010;57:241–292.
8. Tal A, Frydman L. Spatial encoding and the single-scan acquisition of high definition MR images in inhomogeneous fields. J Magn Reson 2006;182:179–194.
9. Schmidt R, Frydman L. In vivo 3D spatial/1D spectral imaging by spatiotemporal encoding: a new single-shot experimental and processing approach. Magn Reson Med 2013;70:382–391.
10. Pipe JG. Spatial encoding and reconstruction in MRI with quadratic phase profiles. Magn Reson Med 1995;33:24–33.
11. Pipe JG. Analysis of localized quadratic encoding and reconstruction. Magn Reson Med 1996;36:137–146.
12. Bruder H, Fischer H, Reinfelder HE, Schmitt F. Image reconstruction for echo planar imaging with nonequidistant k-space sampling. Magn Reson Med 1992;23:311–323.
13. Reeder SB, Atalar E, Faranesh AZ, McVeigh ER. Referenceless interleaved echo-planar imaging. Magn Reson Med 1999;41:87–94.
14. Bernstein MA, King KF, Zhou XJ. Handbook of MRI pulse sequences. Amsterdam: Academic Press; 2004. 1017 p.
15. Chen N, Wyrwicz AM. Removal of EPI Nyquist ghost artifacts with two-dimensional phase correction. Magn Reson Med 2004;51:1247–1253.
16. Hu X, Kim SG. Reduction of signal fluctuation in functional MRI using navigator echoes. Magn Reson Med 1994;31:495–503.
17. Hu X, Le TH. Artifact reduction in EPI with phase-encoded reference scan. Magn Reson Med 1996;36:166–171.
18. Buonocore MH, Gao L. Ghost artifact reduction for echo planar imaging using image phase correction. Magn Reson Med 1997;38:89–100.

19. Buonocore MH, Zhu DC. Image-based ghost correction for interleaved EPI. Magn Reson Med 2001;45:96–108.
20. Hennel F. Image-based reduction of artifacts in multishot echo-planar imaging. J Magn Reson 1998;134:206–213.
21. Ben-Eliezer N, Frydman L. Spatiotemporal encoding as a robust basis for fast three-dimensional in vivo MRI. NMR Biomed 2011;24:1191–1201.
22. Chen L, Bao L, Li J, Cai S, Cai C, Chen Z. An aliasing artifacts reducing approach with random undersampling for spatiotemporally encoded single-shot MRI. J Magn Reson 2013;237:115–124.
23. Schmidt R, Frydman L. New spatiotemporal approaches for fully refocused, multislice ultrafast 2D MRI. Magn Reson Med 2014;71:711–722.
24. Zur Y. Two-dimensional phase correction method for single and multishot echo planar imaging. Magn Reson Med 2011;66:1616–1626.